Ultra-Flexible, "Invisible" Thin-Film Transistors Enabled by Amorphous Metal Oxide/Polymer Channel Layer Blends

Xinge Yu, Li Zeng, Nanjia Zhou, Peijun Guo, Fengyuan Shi, Donald B. Buchholz, Q. Ma, Junsheng Yu, Vinayak P. Dravid, Robert P. H. Chang, Michael Bedzyk, Tobin J. Marks,* and Antonio Facchetti**

Metal oxide (MO) semiconductors have attracted considerable attention for next-generation electronic devices because of their high carrier mobilities, even in the amorphous state, and good environmental stability.[1–5] Equally important, the high optical transparency of MO semiconductors can enable fully transparent thin-film transistors (TFTs), which are essential for the fabrication of "invisible" circuits and to increase the aperture ratio of active-matrix organic light-emitting diode (AMOLED) and liquid-crystal (LC) displays.[6–10] Therefore, since the first report of a fully transparent MO-based TFT in 2003,[13] extensive academic and industrial efforts have focused on enhancing device performance for both opaque and transparent applications.[11,12] Nevertheless, the best performing MO TFTs are typically fabricated by capital-intensive physical and chemical vapor deposition processes. Thus, a key issue for inexpensive large-scale roll-to-roll production is to enable MO TFT manufacturing with solution-based process methodologies. Another key feature of amorphous MO semiconductors is tolerance to mechanical stress, a requirement for device fabrication and utilization on flexible substrates.[11,14,15] Indeed, it is well known that polycrystalline materials have limited mechanical flexibility, mainly due to crack formation at grain boundaries, resulting in dramatic deterioration of the film electrical properties and structural integrity.[16–19]

A well-known strategy to produce amorphous MOs is to dope polycrystalline materials such as indium oxide (In_2O_3) with various X cations, e.g., X = Ga^{3+}, Zn^{2+}, La^{3+}, Sc^{3+}, to form ternary or quaternary amorphous alloys of formula IXO and IXZO (Z = zinc). An example of a technologically relevant amorphous IXZO material is indium–gallium–zinc oxide (IGZO), which has excellent charge transport uniformity due to minimal structural defects.[20–22] However, the carrier mobilities of these amorphous oxides are limited compared to that of the pristine In_2O_3 matrix. Efficient transport in In_2O_3 mainly originates from the diffuse In 5s orbitals at the bottom of the conduction band, edge-sharing In–O_6 octahedra.[23–25] In contrast, the oxygen vacancies regulating the carrier concentrations are difficult to control in In_2O_3, thus the resulting TFTs exhibit less than optimum current modulation (I_{on}/I_{off}) and poor threshold voltage (V_T) uniformity over large areas.[26–28] Furthermore, solution-processed amorphous IXO- and IXZO-based TFTs not only exhibit lower electron mobilities than In_2O_3, but also require relative higher processing temperatures (typically ≥ 300 °C) to facilitate metal–oxygen–metal (M–O–M) lattice formation, densification, and impurity removal[29–33] – temperatures that are incompatible with inexpensive plastic substrates. Consequently, a fundamental challenge in flexible MO electronics is to achieve metal oxide films and electronic devices processed at low temperatures, yet exhibiting transport characteristics comparable to polycrystalline MO semiconductors and having mechanical flexibility of typical amorphous films.[34,35]

In this contribution, we report the first demonstration of solution-processed amorphous In_2O_3 films achieved by doping with an insulating polymer [poly(4-vinylphenol) (PVP)],[36–39] affording high-performance, transparent, and ultra-flexible TFTs at processing temperatures as low as 225 °C. PVP was selected due to the excellent solubility of this polymer in the In_2O_3 precursor formulation solution as well as the presence of hydroxyl groups which should favor coordination to the MO lattice. These devices are fabricated on flexible amorphous ZITO-coated AryLite polyester substrates[40,41] exhibiting high transparency (>80%) and low sheet resistance (<20 Ω $\square^{-1}$). TFTs based on In_2O_3:PVP semiconductor composites having a solution-grown amorphous alumina (AlO_x) gate dielectric ($C_i \approx 90$ nF cm^{-2}) and ZITO source/drain contacts exhibit

X. Yu, Prof. T. J. Marks, Prof. A. Facchetti
Department of Chemistry
Northwestern University
2145 Sheridan Road, Evanston, IL 60208, USA
E-mail: t-marks@northwestern.edu;
a-facchetti@northwestern.edu

X. Yu, Prof. J. Yu
State Key Laboratory of Electronic Thin Films and Integrated Devices
School of Optoelectronic Information
University of Electronic Science and Technology of China (UESTC)
Chengdu 610054, China

L. Zeng
Applied Physics Program and the Materials Research Center
Northwestern University
2220 Campus Dr., Evanston, IL 60208, USA

N. Zhou, P. Guo, Dr. F. Shi, Dr. D. B. Buchholz,
Prof. V. P. Dravid, Prof. R. P. H. Chang, Prof. M. Bedzek
Department of Materials Science and Engineering
the Materials Research Center
Northwestern University
2220 Campus Dr., Evanston, IL 60208, USA
E-mail: bedzyk@northwestern.edu

Dr. Q. Ma
Argonne National Lab
9700 South Cass Avenue, Lemont, IL 60439, USA

Prof. A. Facchetti
Polyera Corporation
8045 Lamon Avenue, Skokie, IL 60077, USA

DOI: 10.1002/adma.201405400

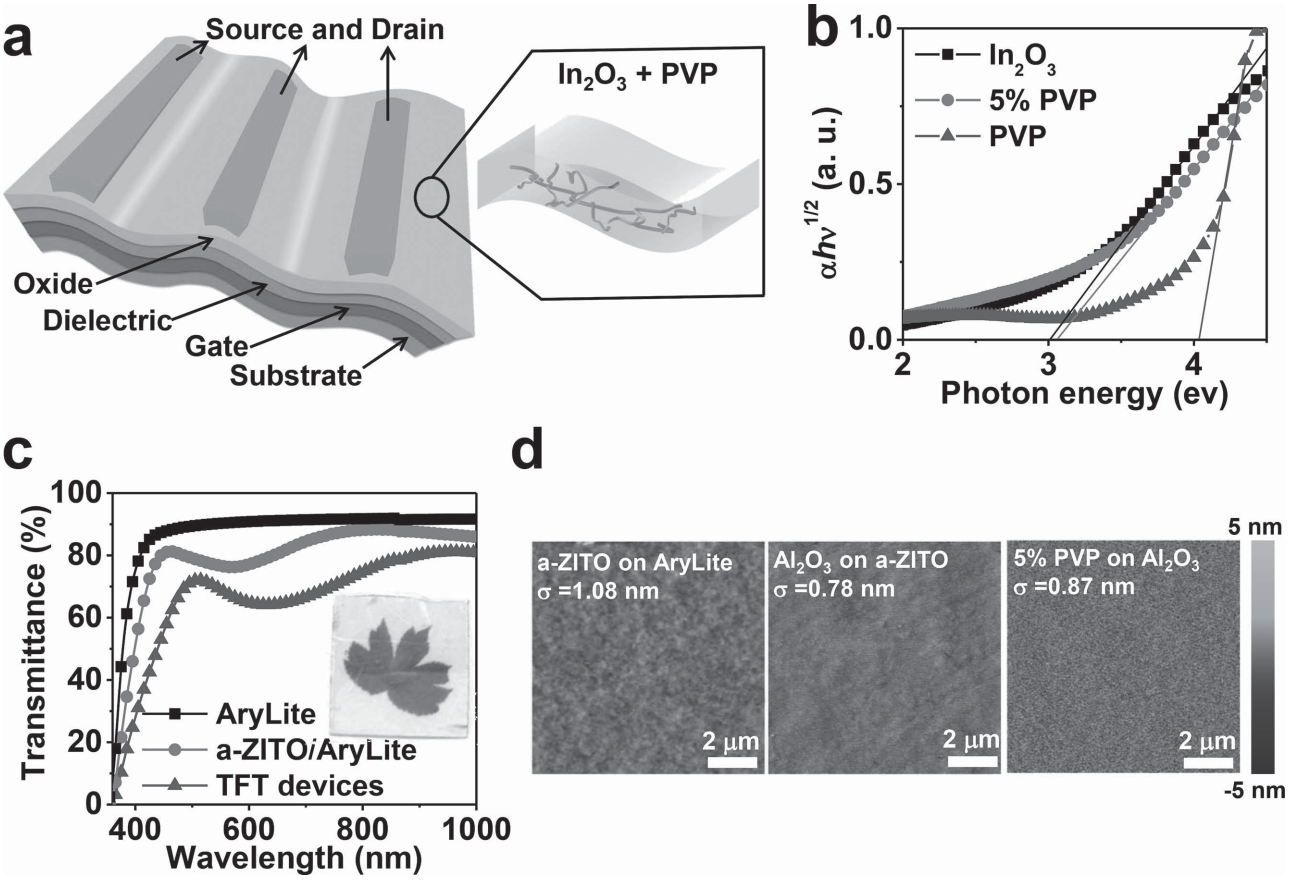

Figure 1. a) Schematic representation of the flexible, transparent TFT structure based on a metal oxide:polymer (In_2O_3:*x*%PVP) semiconductor blend. b) Bandgap extraction from the absorption coefficient versus photon energy. c) Optical transmittance spectra of the AryLite substrate, a-ZITO coated AryLite, and the entire TFT stack; the inset shows the optical image of a TFT array on top of a leaf image. d) AFM images of a-ZITO on an AryLite substrate, AlO_x on top of an a-ZITO-coated AryLite substrate, and In_2O_3:5%PVP on an AlO_x/a-ZITO/AryLite substrate.

electron mobilities >10 $cm^2\ V^{-1}\ s^{-1}$ for 3 V operation. These mobilities are among the highest reported to date for solution-processed transparent MO TFTs and, most importantly, are unchanged upon multiple bending through a radius of 10 mm.

Figure 1a shows a schematic representation of the present flexible MO TFTs having a bottom-gate top-contact architecture. An AryLite plastic is chosen as the substrate due to its exceptionally high optical transparency and good thermal stability.[41] Based on previous experience, a 200 nm thick amorphous $Zn_{0.3}In_{1.4}Sn_{0.3}O_3$ (a-ZITO) film was deposited on Arylite by pulsed laser deposition (PLD) to function as the gate electrode. Next, an AlO_x gate dielectric (k = 9.5, 93 nm thick by profilometry) was deposited on the a-ZITO gate electrode by spin-coating/annealing of an $Al(NO)_3$ precursor solution. The channel layer, consisting of a *x*% by weight PVP-doped In_2O_3 blend [In_2O_3:*x*% PVP; x = 1–20%] was deposited by low-temperature combustion synthesis[42] from a spin-coated PVP–In_2O_3 precursor solution (for details, see the Experimental Section). Next, the spin-coated films were annealed at 225 or 250 °C. Finally, 150 nm thick a-ZITO source/drain electrodes were deposited by PLD through a shadow mask (channel length L = 50 μm, channel width W = 1 mm).

The newly developed In_2O_3:*x*%PVP semiconducting films were first characterized by optical spectroscopy. From the tangent line of the optical absorption α versus photon energy curves (Figure 1b and Figure S1, Supporting Information), the bandgap (E_g) of a 225 °C annealed In_2O_3 film is determined to be 3.01 eV, in agreement with literature values for neat In_2O_3 films.[25] Optimal In_2O_3 blends having a 5% PVP content (In_2O_3:5%PVP), which is the composition giving the best TFT results (vide infra), show a slightly higher E_g of ca. 3.07 eV, probably due to the introduction of the high bandgap (>4 eV) polymer.[43] The average transmittance values of the AryLite substrate and of the a-ZITO/AryLite film are about 90% and 81% in the visible range (400–700 nm), respectively. Importantly, the average transmittance of a 1.5 cm × 1.5 cm TFT array comprising a ZITO/In_2O_3:5% PVP/AlO_x/a-ZITO/AryLite stack is ca. 76%, as shown in Figure 1c. An optical image of the corresponding TFT array is shown as the inset of Figure 1c, also demonstrating the good optical transparency.

The film morphology of both the dielectric and the semiconductor layers plays a critical role in TFT performance since it can strongly affect the charge carrier conducting channel of the devices.[42] Thus, 10 μm × 10 μm atom force microscopy (AFM) images were acquired for a-ZITO films on AryLite, AlO_x films on a-ZITO, and representative In_2O_3:5%PVP films on AlO_x annealed at 225 °C (Figure 1d), revealing smooth, featureless

Adv. Mater. **2015**,
DOI: 10.1002/adma.201405400

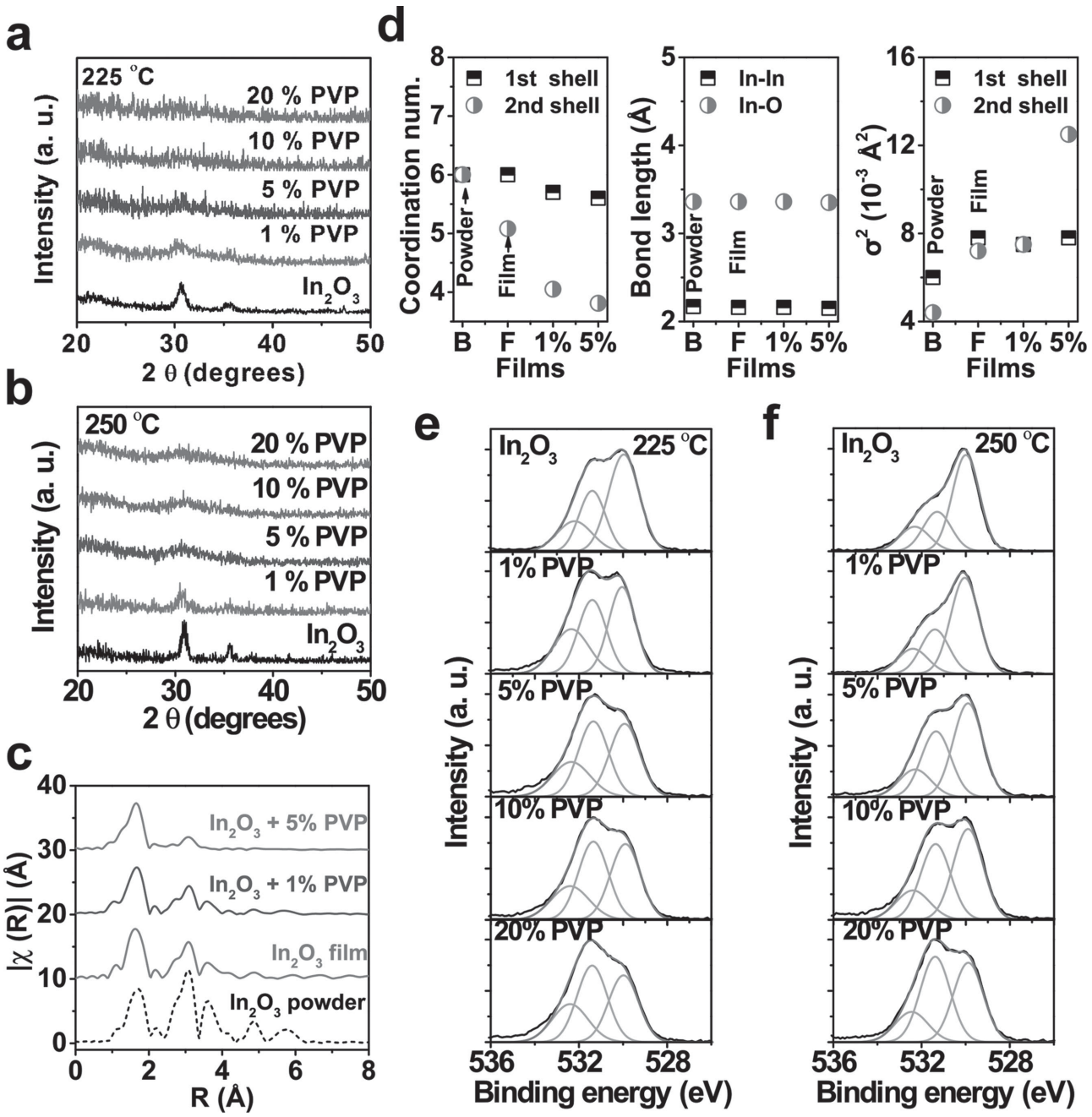

Figure 2. a,b) X-ray diffraction (XRD) patterns of In_2O_3:polymer films with various PVP concentrations: annealing at 225 °C (a), annealing at 250 °C (b). c) Comparison of the In K-edge *p*-RDFs of In_2O_3 powder, a neat In_2O_3 film, In_2O_3:polymer films with 1% and 5% PVP concentrations. d) Derived coordination numbers, In–O bond lengths, and σ^2 values for the indicated films. e,f) X-ray photoelectron spectroscopy (XPS) of In_2O_3:polymer films deposited with various PVP concentrations: annealing at 225 °C (e), annealing at 250 °C (f).

morphologies characterized σ_{RMS} values of 1.08, 0.78, and 0.87 nm, respectively. According to our previous report,[41] the σ_{RMS} of AryLite substrates is ca. 1.1 nm, and here the smoother films with σ_{RMS} < 1 nm for both the dielectric and the blend films is due to the planarization effect of the spin-coating deposition. Nevertheless, the In_2O_3:*x*%PVP films are rougher (σ_{RMS} from 0.39 to 2.19 nm) when the PVP concentration in the blend increases from 0% to 20% by weight (Figure S2, Supporting Information).

To investigate how the PVP concentration affects In_2O_3 semiconductor film microstructure, grazing incidence X-ray diffraction (GIXRD) experiments were carried out for different In_2O_3:*x*%PVP blend films. Representative GIXRD plots for these polymer/MO blend films annealed at 225 and 250 °C are shown in **Figure 2**a,b. It is evident that the neat In_2O_3 films are crystalline even for 225 °C annealing, in agreement with our previous combustion synthesis results.[42] When the annealing temperature is increased to 250 °C, sharper and

stronger Bragg reflections are observed, indicating enhanced film crystallinity. Noticeably, the polycrystalline In_2O_3 films become amorphous when PVP is incorporated to form a blend. Thus, 1% by weight PVP appears to frustrate crystallization at 225 °C, whereas a higher annealing temperature of 250 °C requires 5% by weight of polymer doping to retain an amorphous microstructure.

Next, X-ray absorption fine structure (XAFS) measurements were performed to analyze the amorphous In_2O_3:*x*%PVP film microstructures. XAFS is a powerful tool to probe the local environments around atoms of interest and has been widely used to establish structure–properties correlations for amorphous oxides semiconductors.[44] From extended X-ray absorption fine structure (EXAFS), this technique provides information such as coordination numbers (CNs), bond lengths, and Debye–Waller factors from Equation (1): [45]

$$\chi(k) = \sum_i \frac{N_i(\theta)\left|f_i(k)\right|S_0^2}{kR_i^2}\sin\left[2R_ik + \phi_i(k)\right]e^{\frac{-2R_i}{\lambda(k)}}e^{-2\sigma_i^2k^2} \quad (1)$$

$\chi(k)$ is the normalized absorption coefficient; S_0^2 is the intrinsic loss factor; $\exp(-2R_i/\lambda(k))$ is the attenuation factor related to the electron mean free path $\lambda(k)$; N_i and R_i are the CN and bond distance of the *i*th shell of the absorbing atom, respectively; $f_i(k)$ and $\phi_i(k)$ are the backscattering amplitude and the phase shift; $\exp(-2\sigma_i^2k^2)$ is the Debye–Waller factor. The Fourier transform of $\chi(k)$ can generate the pseudo-radial distribution function (p-RDF) around the central atoms. In order to study the effects of PVP doping in In_2O_3 films, neat In_2O_3, In_2O_3:1%PVP, and In_2O_3:5%PVP films processed at 250 °C were analyzed by EXAFS at the indium *K* edge. Figures 2c,d compare the p-RDFs and fitting results from these three films along with those from an In_2O_3 reference powder (from Aldrich) with a two-shell model and fitting range of k = 3–11 Å^{-1}. The first shell CNs of the In–O In_2O_3:polymer films are 5.7 for In_2O_3:1%PVP and 5.6 for In_2O_3:5%PVP, showing slight undercoordination versus CN = 6 for In_2O_3 powder and film samples. For the second shell, CN decreases more significantly, from 6 in the In_2O_3 powder and 5.08 in the neat In_2O_3 film to 4.05 in In_2O_3:1% PVP, and 3.81 in In_2O_3:5%PVP. The reduced CN first and second shells and the increased Debye–Waller factor in the In_2O_3:polymer blends indicates that crystallization is frustrated by PVP addition.[44,45] In metal ion-doped In_2O_3 films, the introduction of secondary metal ions such as Zn and Ga increases local disorder and suppresses film crystallinity.[44] This is evident in the p-RDF data showing that the In–O polyhedra remain relatively intact (in the first shell, the CN ≈ 6) but the In–M coordination is significantly reduced, while from the EXAFS results (CN ≈ 6 in the first shell and reduction of second shell, higher Debye–Waller factor of second shell) it appears that a similar mechanism operates in all the In_2O_3:*x*%PVP blends, where the polymer chains disrupt oxide lattice formation at the nanoscale grain level rather than at the atomic level. Thus, appropriate polymer incorporation promotes the amorphous state but allows a sufficient density of connected InO_x polyhedra for efficient charge transport.

X-ray photoelectron spectroscopy (XPS) was next utilized to better understand the chemical/structural and local bonding differences between the various In_2O_3-based films. The oxygen 1s (O 1s) spectra indicate three different oxygen environments: condensed M–O–M lattice species at 529.9 ± 0.1 eV; bulk and surface metal hydroxide (M–OH) species at 531.3 ± 0.1 eV; and weakly bound (M–OR) species, i.e., H_2O or CO_2 at 532.2 ± 0.1 eV.[46] Figures 2e,f show the O1s spectra for In_2O_3 for various PVP compositions, ranging from 0.0% to 20%. Data of the O1s subpeak ratios for the lowest energy M–O–M peak, M–OH, and highest energy M–OR peak areas to the total O1s peak area are summarized in Table S2, Supporting Information. Here it can be seen that M–O–M lattice species decrease from 52.6% to 35.4% as the PVP content increases from 0.00% to 20% for 225 °C processing, and from 56.7% to 40.2% for 250 °C processing. Simultaneously, the M–OH content increases with increasing the PVP concentration probably due to the enhanced –OH rich PVP content as well as reduction of contiguous M–O–M domain size. It is generally accepted that the charge transport in MO semiconductors relies on extensive M–O–M lattice network formation, while M–OH species and weakly bound species such as M–OR can act as electron traps.[21,44] Note that greater M–O–M lattice content in In_2O_3 also reflects higher crystallinity in most cases.[42] Although sizable M–O–M content in MO films is essential for efficient charge transport, the electrical performance of crystalline MO films may nevertheless suffer from electrical inhomogeneities, structural defects, and film cracking on flexible substrates, caused by grain boundaries.[26] Furthermore, the edge-sharing In–O_6 octahedra structural nature of In_2O_3 can result in poor control of carrier densities, leading to high off-currents in TFT devices.[24,25,28] Therefore, an accurate balance between M–O–M and M–OH/M–OR content may help control the carrier densities. Thus, the optimal PVP content in our blends for TFT applications (vide infra) is plausibly a compromise between M–O–M content, connectivity between In_2O_3 nanograins, and mechanical stress tolerance.

Another important question addressed using XPS and Fourier transform infrared (FTIR) spectroscopy is whether PVP is stable to the highly exothermic combustion process affording the MO film or whether a substantial quantity of oxidation/decomposition byproducts accumulate in the blend. Thus, XPS carbon 1s (C 1s) spectra of PVP, In_2O_3, and In_2O_3:PVP blend films were next investigated (Figure S3, Supporting Information) From the literature, the PVP C 1s peak has contributions from aromatic carbon–carbon bonds (ca. 284.5 eV), carbon–carbon single bonds of the polymer backbone (ca. 285.0 eV), and carbon–oxygen single bonds (ca. 286.2 eV),[47,48] which are identifiable in our PVP control sample (see Figure S2, Supporting Information). In pure In_2O_3 films only a very weak C 1s feature is observed at a binding energy of ca. 288.6 eV, which can be attributed to adventitious surface contamination arising from carbon oxides or weakly bound organic species.[49,50] In contrast, the XPS data for the In_2O_3:PVP blends suggest that, with the exception of the 1% PVP content sample which falls below the current XPS sensitivity limit, the C 1s peaks can be fitted to PVP aromatic, C–C, and C–O bonds and with the intensities increasing with the PVP concentration. However, as a further proof of stability, another set of experiments was conducted in which PVP was blended with In_2O_3 precursor solutions without fuel, thus avoiding the combustion process, and

Adv. Mater. **2015**,
DOI: 10.1002/adma.201405400

the corresponding films were characterized by XPS (Figure S3c, Supporting Information). The results suggest that the PVP macromolecules are largely retained through the 225 and 250 °C combustion processing and, equally important, PVP does not act as a fuel in these formulations. Moreover, FTIR spectroscopy was performed to further probe for any structural changes in the PVP skeleton. Figures S4 and S5, Supporting Information, show the IR spectra of pure PVP and In_2O_3:PVP blend films after processing at two different temperatures. In all samples, the PVP hydroxyl band diagnostic of H-bonded hydroxyl groups (3360 cm^{-1}) and free hydroxyl groups (3520 cm^{-1})[51] is identical. In addition to the hydroxyl stretching modes, another characteristic PVP bands around 1020 cm^{-1}, assignable to aromatic ring modes, are observed in both pure PVP and in the In_2O_3:PVP blend films, providing further evidence of the PVP oxidative stability.[51,52] This result can be qualitatively ascribed to the endothermic M–O–M lattice formation acting as heat absorber and the ultra-thin film oxide thickness providing a large radiative area for heat dissipation, which minimizes damage to both the PVP polymer and the plastic substrate.[42]

To investigate how the PVP content affects charge transport in In_2O_3:*x*%PVP films, bottom-gate top-contact TFTs were first fabricated on p+ Si/300 nm SiO_2 wafers with thermally evaporated 40 nm Al as s/d electrodes (channel length L = 50 µm, width W = 1000 µm; see Experimental Section for details). **Table 1** summarizes the major TFT performance parameters, and representative transfer I_{DS}–V_{GS} and output I_{DS}–V_{DS} characteristics for selected devices are shown in **Figure 3**, Figure S6 and S7, Supporting Information. Typical *n*-channel TFT behavior is observed for V_{GS} = 80 V and V_{DS} = 80 V operation, and the data clearly show that neat In_2O_3 TFTs exhibit the highest mobility (μ) of ca. 1.52 $cm^2\ V^{-1}\ s^{-1}$ for processing at 225 °C and 3.20 $cm^2\ V^{-1}\ s^{-1}$ for processing at 250 °C. Note however that the threshold voltage V_Ts shift negatively (–1.5 to –12.9 V) and the off currents are quite high, 10^{-8}–10^{-6} A. This result reflects the In_2O_3 high carrier concentration arising from the Fermi level proximity to the conduction band minimum (CBM), thus, it is difficult to deplete the carriers in these polycrystalline In_2O_3 films.[28] In contrast, for the polymer-doped devices, as the PVP concentration is increased, both the mobility and the off-current decrease while the V_T shifts to the positive direction (Figure S8, Supporting Information). Thus, for the In_2O_3:1%PVP samples μ = 1.01 $cm^2\ V^{-1}\ s^{-1}$ (V_T = 3.5 V, I_{off} = 10^{-9} A) and 2.43 $cm^2\ V^{-1}\ s^{-1}$ (V_T = –6.8 V, I_{off} = 10^{-9} A) for annealing at 225 and 250 °C, respectively, whereas for the In_2O_3:5%PVP blends μ falls to 0.92 $cm^2\ V^{-1}\ s^{-1}$ (V_T = 6.4 V, I_{off} = 10^{-9}–10^{-10} A) and 2.12 $cm^2\ V^{-1}\ s^{-1}$ (V_T = 1.2 V, I_{off} = 10^{-9}–10^{-10} A) for annealing at 225 and 250 °C, respectively. The V_T and I_{off} enhancement and slight decrease in μ values can be ascribed to carrier concentration modulation from PVP-induced electron traps. Indeed, the subthreshold swing (SS) for the 250 °C processed In_2O_3:5%PVP TFTs also drops from 8.3 V dec^{-1} (neat In_2O_3 TFTs) to 3.7 V dec^{-1}, leading to a decrease of trap density from 2.2×10^{13} to 6.1×10^{12} cm^{-2} $\left[SS \approx \frac{kT\ln 10}{q}\left(1+\frac{qN_{trap}}{C_i}\right)\right]$. As a result, V_T and I_{off} performance for the In_2O_3:5%PVP devices is enhanced. However, further increase of the PVP concentration dramatically lowers the electron mobility to 0.54 $cm^2\ V^{-1}\ s^{-1}$ at 225 °C and 1.49 $cm^2\ V^{-1}\ s^{-1}$ at 250 °C for In_2O_3:10%PVP, and 0.04 $cm^2\ V^{-1}\ s^{-1}$ at 225 °C and 0.16 $cm^2\ V^{-1}\ s^{-1}$ at 250 °C for In_2O_3:20%PVP devices. Furthermore, the transport characteristics also indicate that the *I*–*V* hysteresis increases with increasing the PVP concentration, likely due to increased trap density arising from the large densities of residual OH groups as well as the disruption of conduction pathways, as supported by the EXAFS experiments (see below).

By combining the microstructural and TFT performance results, it is concluded that a 5% PVP content in the In_2O_3:*x*%PVP blend is the optimum composition, which not only provides acceptable TFT performance, but also the formation of an amorphous microstructure. Encouraged by the successful TFT data obtained on Si/SiO_2 substrates, the TFT performance was further optimized by device engineering. Thus, n^{++}-Si was employed as gate electrodes/substrates, a spin-coated 93 nm thick AlO_x film as the gate dielectric layer, with a unit capacitance of 90.5 nF cm^{-2} (Figure S9, Supporting Information), and a In_2O_3:5%PVP as the MO semiconductor, to further enhance the device performance at low operating voltage. The resulting $Si/AlO_x/In_2O_3$:5%PVP TFTs exhibit substantial performance with $\mu \approx 16.5$ $cm^2\ V^{-1}\ s^{-1}$, $V_T \approx 0.6$ V, and $I_{on}/I_{off} \approx 10^5$ for annealing at a 225 °C (Figure 3d). The performance improvement is ascribed to the reduction of dielectric/MO semiconductor interfacial traps, and agrees with the knowledge that high capacitance dielectrics improve metal oxide TFT performance.[53,54] When replacing Si with AryLite polyester as the substrate and a-ZITO as both the gate and source/

Table 1. Performance metrics for MO:PVP TFTs with different concentrations of PVP.[a)]

T_a [°C]	TFT performance	PVP concentration [%]				
		0	1	5	10	20
225	μ [$cm^2\ V^{-1}\ s^{-1}$]	1.52 ± 0.06	1.01 ± 0.06	0.92 ± 0.07	0.54 ± 0.05	0.04 ± 0.02
	V_T [V]	2.8 ± 2.4	3.5 ± 2.6	6.4 ± 3.8	22.7 ± 3.5	28.6 ± 4.9
	I_{on}/I_{off}	10^4–10^5	10^5–10^6	10^5–10^6	10^5–10^6	10^5–10^6
250	μ [$cm^2\ V^{-1}\ s^{-1}$]	3.20 ± 0.10	2.43 ± 0.14	2.12 ± 0.11	1.49 ± 0.09	0.16 ± 0.08
	V_T [V]	–12.9 ± 1.6	–6.8 ± 1.8	1.2 ± 1.7	14.5 ± 2.4	25.1 ± 3.5
	I_{on}/I_{off}	10^3–10^4	10^5–10^6	10^6–10^7	10^4–10^5	10^5–10^6

[a)]Each device metric is the average of a minimum of 15 devices.

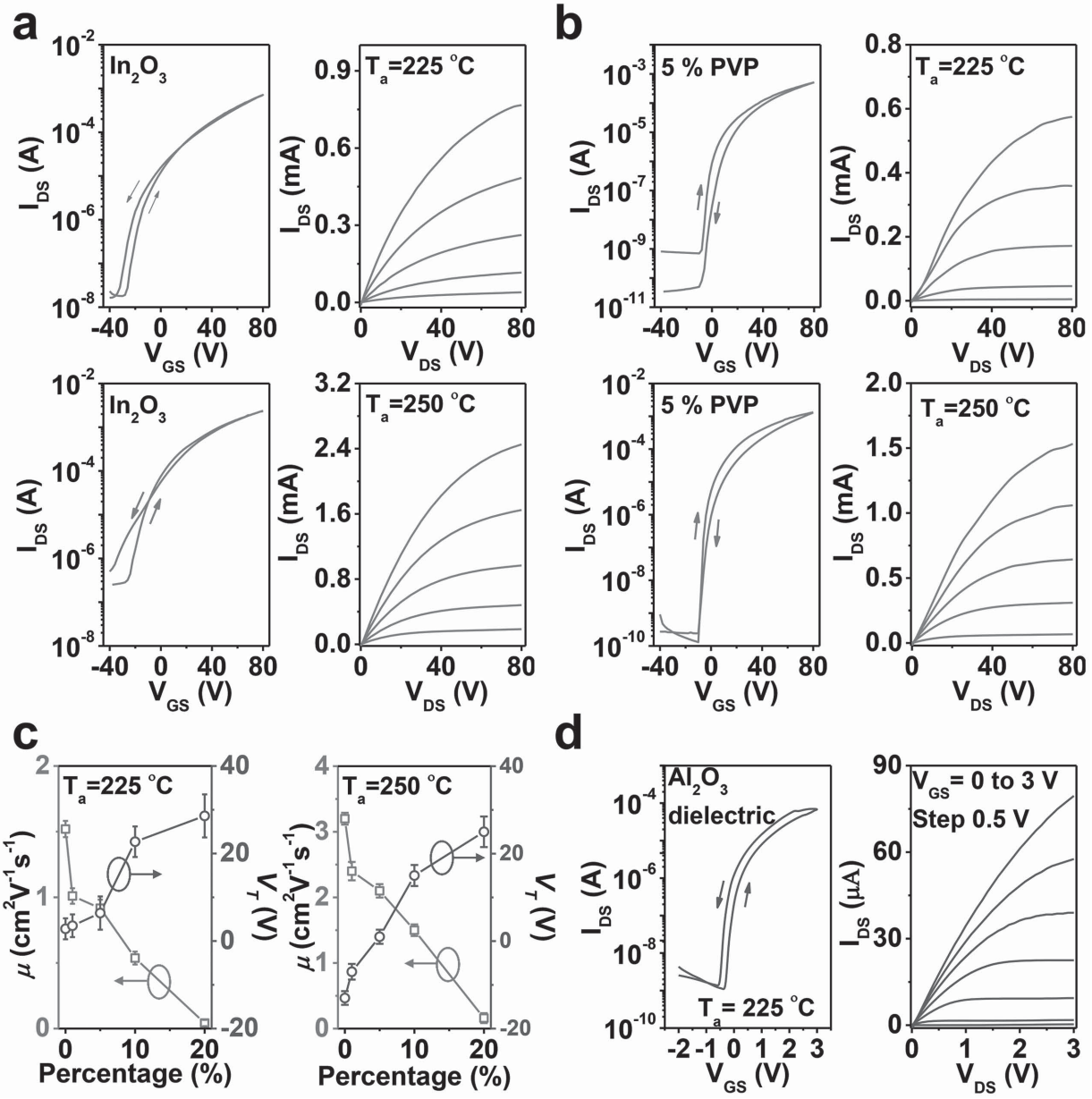

Figure 3. Representative transfer and output characteristics for metal oxide TFTs fabricated on 300 nm SiO_2/Si substrates: a) Neat In_2O_3 semiconductor devices, b) In_2O_3:5% PVP semiconductor. c) TFT mobility and threshold voltage for In_2O_3:polymer films having different PVP concentrations, processed at 225 and 250 °C. d) Transfer and output characteristics of a TFT with a structure of Si/AlO_x/In_2O_3:5% PVP/Al.

drain electrodes, an "invisible" and flexible TFT (optical image shown in Figure 1c) with the structure AryLite/a-ZITO/AlO_x/In_2O_3:5%PVP/a-ZITO is achieved, exhibiting the following performance: $\mu \approx 10.9$ cm^2 V^{-1} s^{-1}, $V_T \approx 0.7$ V, and $I_{on}/I_{off} \approx 10^5$ (Figure 5a,b).

Next, cross-sectional transmission electron microscopy (TEM) was performed to investigate the microstructures of the best-performing flexible devices in greater detail. Thus, In_2O_3/5%PVP coated AlO_x/a-ZTIO/AryLite samples were prepared for analysis with focused ion beam (FIB) techniques. As shown in **Figure 4**a, this sample reveals well-defined layers, all having uniform thickness across the entire sample area, and the top view bright-field TEM image of a In_2O_3:5% PVP film is shown in Figure 4d. Figure 4b shows an energy-dispersive X-ray spectroscopy (EDS) scan in the indicated area of Figure 4a for Al, In, Sn, and Zn. The elemental distribution indicates a continuous layer-by-layer structure. The energy-filtered nanobeam diffraction (EF-NBD) patterns of a-ZITO, AlO_x, and In_2O_3:5%PVP film all show typical "halo rings" characteristic of amorphous films (Figure 4c). Such results further corroborate that both the ZITO and AlO_x films are amorphous after 225 °C annealing, in agreement with the XRD data shown in Figures S10 and S11, Supporting Information. The amorphous feature for all these films is very important for mechanical flexibility.

Adv. Mater. **2015**,
DOI: 10.1002/adma.201405400

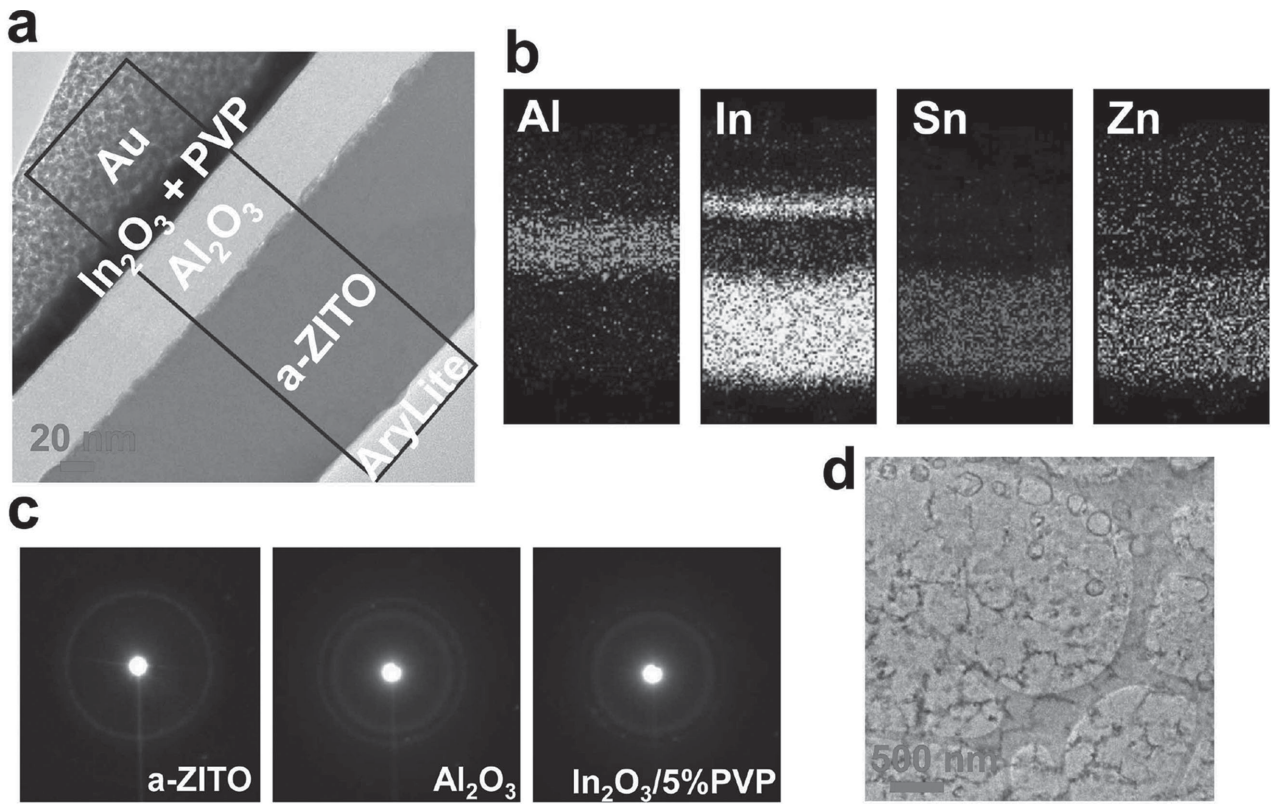

Figure 4. a) Cross-section TEM images of a flexible TFT device with the structure: AryLite/a-ZTIO/AlO_x/In_2O_3:5% PVP/Au (T_{ann} = 225 °C). b) EDS analysis of Al, In, Sn, and Zn elements within the black box indicated in (a). c) EF-NBED pattern of a-ZITO, AlO_x, and In_2O_3:5% PVP, the resolution of diffraction nanobeam is 1 nm. d) Top view of TEM morphology of a In_2O_3:5% PVP In_2O_3 film.

To systematically characterize the mechanical flexibility of the present all-transparent In_2O_3:5%PVP devices, a series of bending tests under controlled conditions were performed (Figure S12, Supporting Information). As a comparison, an all-transparent TFTs based on neat In_2O_3 as the semiconductor were also measured. **Figure 5**a shows the transfer plots of these devices at various bending radii along a curvature parallel to the channel length. Clearly, the mobility of neat In_2O_3 TFT deteriorates significantly from 22.2 (before bending) to 0.5 $cm^2\ V^{-1}\ s^{-1}$ as the bending radius is decreased to 10 mm, and a large V_T shift from +0.7 to +1.9 V is also observed. On further decreasing the bending radius to 7 mm, the neat In_2O_3 TFT no longer exhibits a transistor response (Figure 5c). In contrast, TFT devices based on amorphous In_2O_3:5%PVP as the semiconductor exhibit only a slight V_T shift from +0.6 to +1.2 V as the bending radius is decreased to 10 mm, along with a negligible mobility decline from 10.9 to 8.9 $cm^2\ V^{-1}\ s^{-1}$ (Figure 5a,c). In regard to the mobility dependence on the number of bending cycles shown in Figure 4c, the corresponding In_2O_3:PVP TFTs show excellent mechanical flexibility with negligible performance decease upon bending at 10 mm to up to 100 times (Figure 5c). Moreover, the transfer and output characteristics of In_2O_3:5%PVP TFTs almost completely recover when the strain is relaxed, as shown in Figure 5b. The performance deterioration upon mechanical stress is attributed to crack formation within the MO channel, as clearly observed by analyzing the channel film topology using SEM (Figure 5d and Figure S12, Supporting Information). Thus, SEM images of 20 nm thick In_2O_3/AryLite and In_2O_3:5%PVP/AryLite films (225 °C) after 100 bending cycles at 10 mm radii indicate extensive crack formation and propagation for the polycrystalline film whereas that of the In_2O_3:5%PVP remain continuous and uniform.

In conclusion, we have successfully developed a new low temperature route (as low as 225 °C) to high-mobility amorphous metal oxide semiconductor films via doping with an insulating polymer to afford amorphous MO:polymer blend composites. Such an approach effectively frustrates crystallization, controls the carrier concentration in the In_2O_3 channel, and retains conducting pathways for efficient charge transport. By using AryLite substrates and transparent dielectric/contact materials, all-amorphous and "invisible" TFTs are demonstrated which also exhibit excellent mechanical flexibility. Thus, In_2O_3:5%PVP TFTs exhibit electron mobilities approaching 11 $cm^2\ V^{-1}\ s^{-1}$ before mechanical stress, and they can retain up to ca. 90% of their performance upon bending/relaxing (r = 10 mm) 100 times. This work demonstrates that polymer doping of metal oxides not only opens a new route to low temperature high-mobility amorphous semiconductors, but also achieves mechanical stress tolerance, essential for the next-generation of ultraflexible circuits.

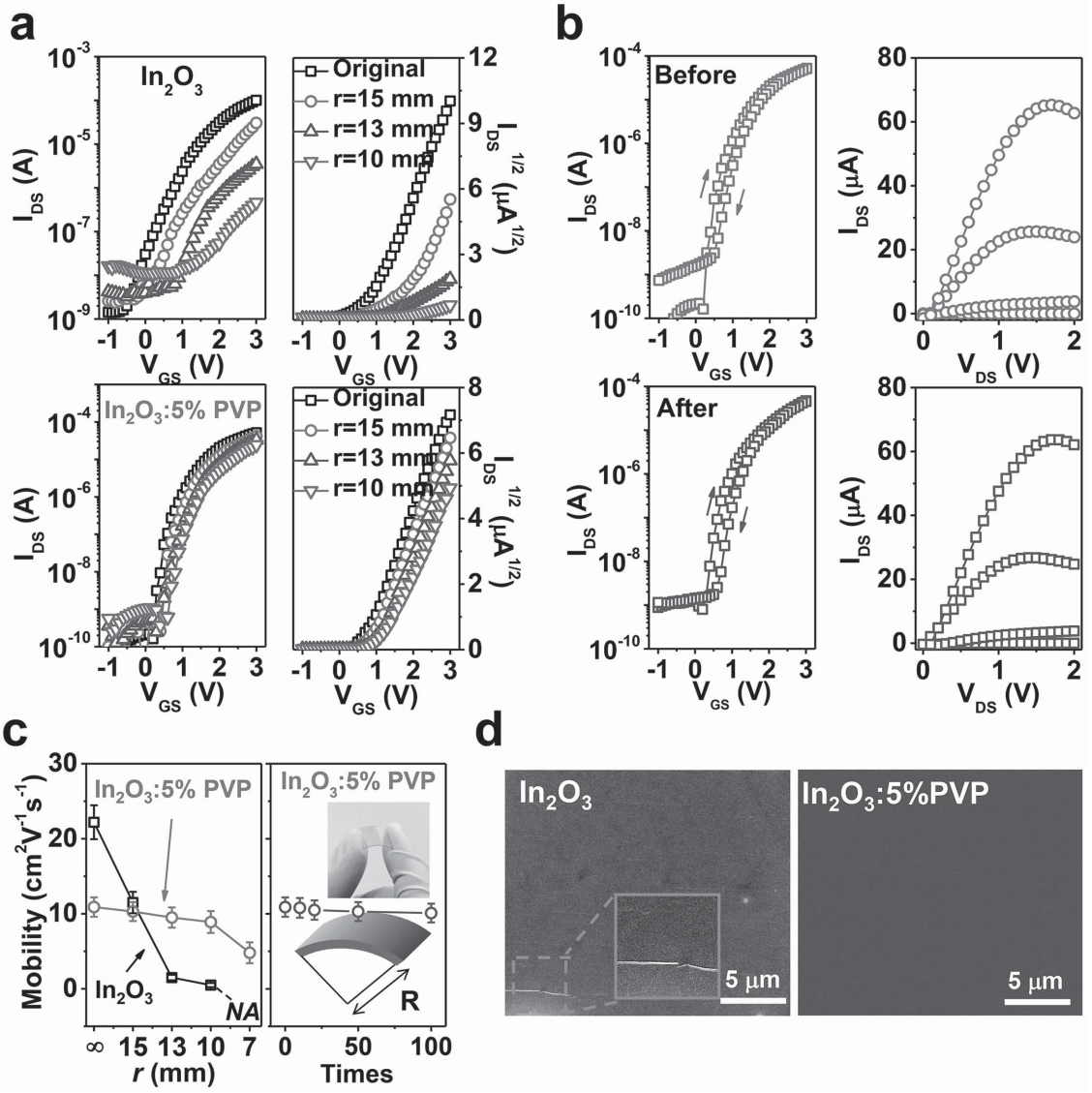

Figure 5. a) Bending dependence of transfer curves for neat In_2O_3 TFTs and all-amorphous In_2O_3:5% PVP TFTs before and during various bending radius tests. b) Representative output and transfer plots of identical all-amorphous MO: polymer TFTs before and after 100 bending cycles at a radius of 10 mm. c) Dependence of TFT mobilities on bending radius of both neat In_2O_3 TFTs and all-amorphous In_2O_3:5% PVP TFTs (left), and mobilities on all-amorphous TFT bending cycles at a radius of 10 nm. Inset: Optical image of transparent flexible TFTs. d) SEM images of 20 nm In_2O_3 and In_2O_3:5% PVP films on AryLite processed at 225 °C, after 100 bending cycles at a radius of 10 mm. The TFTs were fabricated with the architecture AryLite/a-ZTIO/AlO_x/In_2O_3:5% PVP/a-ZITO, annealed at 225 °C.

Experimental Section

Precursor Solutions: In_2O_3 combustion precursor solutions were prepared according to the following procedure: 177.4 mg of $In{\cdot}(NO_3)_3{\cdot}xH_2O$ was dissolved in 10 mL of 2-methoxyethanol before the addition of 55 μL of NH_4OH and 100 μL of acetylacetone and allowed to stir overnight. PVP (Sigma–Aldrich $M_W \approx 25\,000$ g mL^{-1}) was also dissolved by stirring in 2-methoxyethanol overnight to form a 10 mg mL^{-1} solution. The In_2O_3:solution polymer precursor solutions were prepared by adding the PVP solution to the In_2O_3 precursor solution so as to achieve a PVP weight fraction content (*x*%) from 1% to 20%. After addition, these solutions were stirred for 4 h before deposition. The alumina dielectric precursor solution was prepared by dissolving $Al{\cdot}(NO_3)_3{\cdot}xH_2O$ in 2-methoxyethanol to achieve a 0.25 M solution, and then stirred overnight before deposition. All the reagents were from Sigma-Aldrich and were used as received.

Transistor Fabrication and Electrical Characterization: For rigid silicon substrates, doped silicon wafers with a 300 nm thermal SiO_2 layer (WRS Materials; solvent cleaned and then treated with an oxygen plasma for 5 min) were used as the gate electrode and dielectric layer, respectively. The semiconductor solutions were deposited by spin-coating at 3500 rpm for 30 s, and then annealed on a hot plate at temperatures of 225 or 250 °C for 30 min. This process was repeated four times to achieve desire thickness, the resulted thicknesses are about 18 nm for neat In_2O_3, and 18–23 nm for In_2O_3:*x*%PVP depending on the contents of PVP. For the all-transparent TFTs, amorphous AlO_x solutions were spin-coated onto a-ZITO coated 100 μm Arylite polyester sheets (see ref. [42] for details) and then annealed at 200 °C for 30 min, this process was repeated

Adv. Mater. **2015**,
DOI: 10.1002/adma.201405400

three times. Finally, 150 nm a-ZITO source and drain electrodes were deposited onto MO films through a shadow mask. The channel length and width for all devices in this study were 50 and 1000 μm, respectively. TFT characterization was performed under ambient conditions on a custom probe station using an Agilent 1500 semiconductor parameter analyzer. The charge carrier mobility μ was evaluated in the saturation region with the conventional metal–oxide–semiconductor field-effect transistor (MOSFET) model by the following equation:

$$I_{DS} = (WC_i / 2L)\mu(V_{GS} - V_T)^2 \quad (2)$$

where C_i is the capacitance per unit area of insulator, V_T is the threshold voltage, and V_{GS} is gate voltage. W and L are the channel width and length, respectively.

Oxide Film Characterization: AFM film morphologies were imaged with a Veeco Dimension Icon scanning Probe Microscope using tapping mode. GIXRD measurements were performed with a Rigaku ATX-G Thin Film Diffraction Workstation using Cu K_α radiation coupled to a multilayer mirror. XAFS were conducted with a sector 5BMD. Cross-sectional TEM measurements were performed using a JEOL JEM-2100F instrument, with samples prepared directly from actual devices using FIB techniques (FEI Helios NanoLab 600). A thin Au layer was locally deposited on the sample to protect from damage during the FIB processing. XPS (Omicron ESCA Probe) characterization of In 3d and O 1s signals was monitored on In_2O_3:PVP/SiO_2 after surface cleaning.

Supporting Information

Supporting Information is available from the Wiley Online Library or from the author.

Acknowledgements

The authors thank Polyera Corp., ONR (MURI N00014-11-1-0690), and the Northwestern University Materials Research Science and Engineering Center (NSF DMR-1121262) for support of this research. Microscopy studies were performed in the NIFTI and KECK II facilities of NUANCE Center at Northwestern University, and Argonne National Lab. NUANCE is supported by NSF-NSEC, NSF-MRSEC, Keck Foundation, the State of Illinois, and Northwestern University.

Figure 3 and 5 were reset after initial publication online.

Received: November 25, 2014
Revised: January 24, 2015
Published online:

[1] K. Nomura, H. Ohta, A. Takagi, T. Kamiya, M. Hirano, H. Hosono, *Nature (London)* **2004**, *432*, 488.
[2] D. B. Buchholz, Q. Ma, D. Alducin, A. Ponce, M. Yacaman, R. Khanal, J. E. Medvedeva, R. P. H. Chang, *Chem. Mater.* **2014**, *26*, 5401.
[3] Y. H. Kim, J. S. Heo, T. H. Kim, S. Park, M. H. Yoon, J. Kim, M. S. Oh, G. R. Yi, Y. Y. Noh, S. K. Park, *Nature (London)* **2012**, *489*, 128.
[4] K. K. Banger, Y. Yamashita, K. Mori, R. L. Peterson, T. Leedham, J. Rickard, H. Sirringhaus, *Nat. Mater.* **2011**, *10*, 45.
[5] S. R. Thomas, P. Pattanasattayavong, T. D. Anthopoulos, *Chem. Soc. Rev.* **2013**, *42*, 6910.
[6] S. Ju, A. Facchetti, Y. Xuan, J. Liu, F. Ishikawa, P. Ye, C. Zhou, T. J. Marks, D. B. Janes, *Nat. Nanotechnol.* **2007**, *2*, 378.
[7] S.-H. K. Park, C.-S. Hwang, M. Ryu, S. Yang, C. Byun, J. Shin, J.-I. Lee, K. Lee, M. S. Oh, S. Im, *Adv. Mater.* **2009**, *21*, 678.
[8] J. Liu, D. B. Buchholz, R. P. Chang, A. Facchetti, T. J. Marks, *Adv. Mater.* **2010**, *22*, 2333.
[9] M. A. McCarthy, B. Liu, E. P. Donoghue, I. Kravchenko, D. Y. Kim, F. So, A. G. Rinzler, *Science* **2011**, *332*, 570.
[10] J. Liang, L. Li, X. Niu, Z. Yu, Q. Pei, *Nat. Photonics* **2013**, *7*, 817.
[11] J. Liu, D. B. Buchholz, J. W. Hennek, R. P. H. Chang, A. Facchetti, T. J. Marks, *J. Am. Chem. Soc.* **2010**, *132*, 11934.
[12] S. Chang, Y. S. Do, J.-W. Kim, B. Y. Hwang, J. Choi, B.-H. Choi, Y.-H. Lee, K. C. Choi, B.-K. Ju, *Adv. Funct. Mater.* **2014**, *24*, 3482.
[13] J. F. Wager, *Science* **2003**, *300*, 1245.
[14] W. Yang, K. Song, Y. Jung, S. Jeong, J. Moon, *J. Mater. Chem. C* **2013**, *1*, 4275.
[15] H. Xu, D. Luo, M. Li, M. Xu, J. Zou, H. Tao, L. Lan, L. Wang, J. Peng, Y. Cao, *J. Mater. Chem. C* **2014**, *2*, 1255.
[16] H. Imai, A. Tominaga, H. Hirashima, M. Toki, N. Asakuma, *J. Appl. Phys.* **1999**, *85*, 203.
[17] D. R. Cairns, R. P. White, D. K. Sparacin, S. M. Sachsman, D. C. Paine, G. P. Crawfordl, R. R. Newton, *Appl. Phys. Lett.* **2000**, *76*, 1425.
[18] C. Peng, Z. Jia, D. Bianculli, T. Li, J. Lou, *J. Appl. Phys.* **2011**, *109*, 103530.
[19] G. Z. Xing, J. B. Yi, F. Yan, T. Wu, S. Li, *Appl. Phys. Lett.* **2014**, *104*, 202411.
[20] S. Jeong, Y.-G. Ha, J. Moon, A. Facchetti, T. J. Marks, *Adv. Mater.* **2010**, *22*, 1346.
[21] J. W. Hennek, J. Smith, A. Yan, M. G. Kim, W. Zhao, V. P. Dravid, A. Facchetti, T. J. Marks, *J. Am. Chem. Soc.* **2013**, *135*, 10729.
[22] K. K. Banger, R. L. Peterson, K. Mori, Y. Yamashita, T. Leedham, H. Sirringhaus, *Chem. Mater.* **2014**, *26*, 1195.
[23] M. Orita, H. Tanji, M. Mizuno, H. Adachi, I. Tanaka, *Phys. Rev. B* **2000**, *61*, 1811.
[24] H.-K. Noh, K. J. Chang, B. Ryu, W.-J. Lee, *Phys. Rev. B* **2011**, *84*, 115205.
[25] F. Fuchs, F. Bechstedt, *Phys. Rev. B* **2008**, *77*, 155107.
[26] E. Fortunato, P. Barquinha, R. Martins, *Adv. Mater.* **2012**, *24*, 2945.
[27] K. Ellmer, R. Mientus, *Thin Solid Films* **2008**, *516*, 4620.
[28] X. Yu, N. Zhou, J. Smith, H. Lin, K. Stallings, J. Yu, T. J. Marks, A. Facchetti, *ACS Appl. Mater. Interfaces* **2013**, *5*, 7983.
[29] H. Q. Chiang, B. R. McFarlane, D. Hong, R. E. Presley, J. F. Wager, *J. Non-Cryst. Solids* **2008**, *354*, 2826.
[30] S. K. Park, Y.-H. Kim, J.-I. Han, *J. Phys. D: Appl. Phys.* **2009**, *42*, 2826.
[31] P. K. Nayak, M. N. Hedhili, D. Cha, H. N. Alshareef, *Appl. Phys. Lett.* **1993**, *100*, 202106.
[32] C.-Y. Tsay, T.-Y. Yan, *J. Phys. Chem. Solids* **2014**, *75*, 142.
[33] J. H. Choi, S. M. Hwang, C. M. Lee, J. C. Kim, G. C. Park, J. Joo, J. H. Lim, *J. Cryst. Growth* **2011**, *326*, 175.
[34] D. Wee, S. Yoo, Y. H. Kang, Y. H. Kim, J.-W. Ka, S. Y. Cho, C. Lee, J. Ryu, M. H. Yi, K.-S. Jang, *J. Mater. Chem. C* **2014**, *2*, 6395.
[35] J. H. Cho, J. Lee, Y. Xia, B. Kim, Y. He, M. J. Renn, T. P. Lodge, C. D. Frisbie, *Nat. Mater.* **2008**, *7*, 900.
[36] Y. Lee, H. Y. Park, J. H. Park, G. Yoo, M. H. Lim, J. Park, S. Rathi, W. S. Jung, J. Kim, S. W. Kim, Y. Roh, G. H. Kim, J. H. Park, *Nanoscale* **2014**, *6*, 3830.
[37] T. Q. Trung, N. T. Tien, D. Kim, M. Jang, O. J. Yoon, N.-E. Lee, *Adv. Funct. Mater.* **2014**, *24*, 117.
[38] J. H. Schattka, D. G. Shchukin, J. Jia, M. Antonietti, R. A. Caruso, *Chem. Mater.* **2002**, *14*, 5103.
[39] T. Kato, T. Suzuki, T. Amamiya, T. Irie, M. Komiyama, H. Yui, *Supramol. Sci.* **1998**, *5*, 411.
[40] D. B. Buchholz, J. Liu, T. J. Marks, M. Zhang, R. P. Chang, *ACS Appl. Mater. Interfaces* **2009**, *1*, 2147.
[41] N. Zhou, D. B. Buchholz, G. Zhu, X. Yu, H. Lin, A. Facchetti, T. J. Marks, R. P. Chang, *Adv. Mater.* **2014**, *26*, 1098.

[42] M. G. Kim, M. G. Kanatzidis, A. Facchetti, T. J. Marks, *Nat. Mater.* **2011**, *10*, 382.
[43] R. Abargues, K. Abderrafi, E. Pedrueza, R. Gradess, J. Marqués-Hueso, J. L. Valdés, J. Martínez-Pastor, *New J. Chem.* **2009**, *33*, 1720.
[44] K. Nomura, T. Kamiya, H. Ohta, T. Uruga, M. Hirano, H. Hosono, *Phys. Rev. B* **2007**, *75*, 035212 .
[45] D. E. Proffit, Q. Ma, D. B. Buchholz, R. P. H. Chang, M. J. Bedzyk, T. O. Mason, *J. Am. Ceram. Soc.* **2010**, *95*, 3657.
[46] T. Ishida, H. Kobayashi, Y. Nakato, *J. Appl. Phys.* **1993**, *73*, 4344.
[47] G. Beamson, D. Briggs, *High Resolution XPS of Organic Polymers*, Wiley, Chichester, UK **1992**, p. 152.
[48] Z. Zhang, Z. Mo, H. Zhang, Y. Zhang, T. Na, Y. An, X. Wang, X. Zhao, *J. Polym. Sci., Part B: Polym. Phys.* **2002**, *40*, 1957.
[49] V. B. Crist, *Handbooks of Monochromatic XPS Spectra: The Elements and Native Oxides*, XPS International LLC, Mountain View, CA, USA **2004**.
[50] C. Donley, D. Dunphy, D. Panie, C. Carter, K. Nebesny, P. Lee, D. Alloway, N. R. Armstrong, *Langmuir* **2002**, *18*, 450.
[51] H. Zhang, Z. Wang, Y. Zhang, X. Zhang, *Langmuir* **2004**, *20*, 9366.
[52] S.-W. Kuo, P.-H. Tung, F.-C. Chang, *Macromolecules* **2006**, *39*, 9388.
[53] B. N. Pal, B. M. Dhar, K. C. See, H. E. Katz, *Nat. Mater.* **2009**, *8*, 898.
[54] R. P. Ortiz, A. Facchetti, T. J. Marks, *Chem. Rev.* **2010**, *110*, 205.

Adv. Mater. **2015**,
DOI: 10.1002/adma.201405400